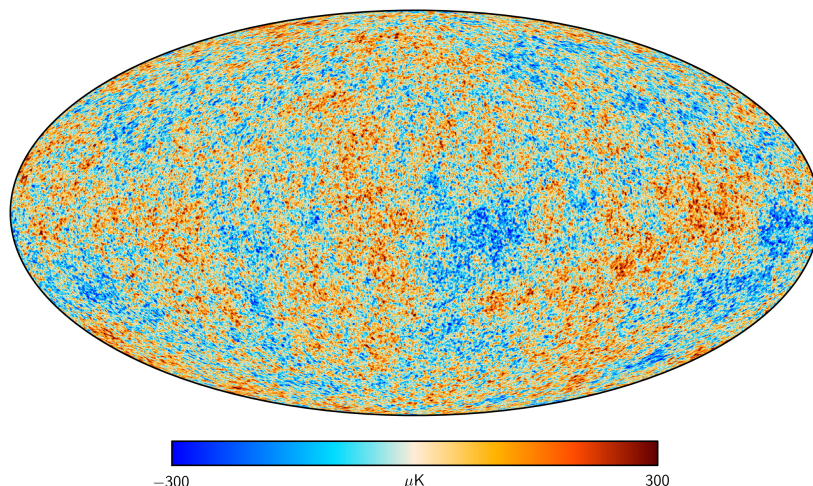# FLUCTUATIONS IN THE COSMIC MICROWAVE BACKGROUND

Figure 10.1: Temperature fluctuations of the Cosmic Microwave Background measured by the Planck collaboration (2015), after subtracting the dipole due to the Earth's motion and the foreground emission from the Milky Way.

We have already mentioned several times that the anisotropies in the temperature of the CMB radiation encode a host of cosmological parameters; this is the attraction that has motivated successive space and ground-based missions over the last fifty years to record the CMB sky with increasing accuracy. In this lecture we shall look a little more closely at the analysis of these fluctuations and the information they provide.

In general terms, we make a distinction between three main categories of effects that cause fluctuations in the temperature (and polarization, which will not be discussed in these lectures) of the CMB. *Primary* fluctuations, imprinted on the surface of last scattering at z_{dec}. These fluctuations reflect density inhomogeneities which are the seeds from which the large-scale structure of the Universe has evolved. They are thought to have their origin from random quantum fluctuations in the very early Universe, subsequently stretched by inflation into cosmic scales. *Secondary* fluctuations are due to the interaction of some CMB photons (at a level of 1 in 10^4–10^5) with matter on their way from the surface of last scattering to the nearby Universe. *Tertiary* fluctuations, also called *foregrounds*, are effects due to

dust and gas in our own Galaxy. In this lecture we will focus on the primary fluctuations, as they are the ones of most interest for cosmology, but we will also consider one important source of secondary fluctuations, the so-called Sunyaev-Zeldovich effect produced by high temperature electrons in the intercluster medium of massive galaxy clusters.

10.1 Statistical Description of the Fluctuations

First of all, when we record the CMB signal from different locations on the sky, the quantity measured is the intensity at a given frequency, I_ν. This can be related to the blackbody temperature as follows. In the low frequency regime (the Raleigh-Jeans portion of the Planck function) we have:

$$I_\nu = \frac{2h\nu^3/c^2}{e^{h\nu/kT} - 1} \tag{10.1}$$

or

$$I_\nu \propto \nu^2 T \qquad \text{when } h\nu \ll kT \tag{10.2}$$

so that:

$$\frac{\delta I_\nu}{I} = \frac{\delta T}{T} \tag{10.3}$$

at a given frequency ν.

In Lecture 9 we defined the temperature fluctuations as:

$$\frac{\delta T}{T}(\theta, \phi) = \frac{T(\theta, \phi) - \langle T \rangle}{\langle T \rangle} \,, \tag{10.4}$$

where θ and ϕ are angular coordinates on the celestial sphere (analogous to latitude and longitude on the surface of the Earth). It is customary the expand these fluctuations in spherical harmonics:

$$\frac{\delta T}{T}(\theta, \phi) = \sum_{\ell=0}^{\infty} \sum_{m=-\ell}^{\ell} a_\ell^m \, Y_\ell^m(\theta, \phi) \tag{10.5}$$

where $Y_\ell^m(\theta, \phi)$ are the usual spherical harmonic functions:

$$Y_0^0(\theta, \phi) = \frac{1}{2}\sqrt{\frac{1}{\pi}}$$

$$Y_1^{-1}(\theta, \phi) = \frac{1}{2}\sqrt{\frac{3}{2\pi}}\,\sin\theta\,e^{-i\phi}$$

$$Y_1^0(\theta, \phi) = \frac{1}{2}\sqrt{\frac{3}{\pi}}\,\cos\theta$$

$$Y_1^1(\theta, \phi) = -\frac{1}{2}\sqrt{\frac{3}{2\pi}}\,\sin\theta\,e^{i\phi}$$

and so on.

A statistical measure of the temperature fluctuations is the correlation function, $C(\theta)$. Consider two points on the surface of last scattering, in directions represented by the vectors $\mathbf{r}$ and $\mathbf{r}'$, separated by the angle θ such that $\cos\theta = \mathbf{r} \cdot \mathbf{r}'$. The correlation function $C(\theta)$ is found by multiplying together the values of $\delta T/T$ at the two points, and averaging the product over all pairs of points separated by the angle θ:

$$C(\theta) = \left\langle \frac{\delta T}{T}(\mathbf{r})\frac{\delta T}{T}(\mathbf{r}') \right\rangle_{\mathbf{r}\cdot\mathbf{r}'=\cos\theta} \tag{10.6}$$

If we knew the value of $C(\theta)$ for all angles θ we would have a complete statistical description of the temperature fluctuations over the entire sky (all angular scales). In practice, however, this information is available only over a limited range of scales. Using the expansion of $\delta T/T$ in spherical harmonics (eq 10.5), the correlation function can be written in the form:

$$C(\theta) = \frac{1}{4\pi}\sum_{\ell=0}^{\infty}(2\ell+1)\,C_\ell\,P_\ell(\cos\theta) \tag{10.7}$$

where P_ℓ are the Legendre polynomials:

$$P_0(x) = 1$$

$$P_1(x) = x$$

$$P_2(x) = \frac{1}{2}(3x^2 - 1)$$

and so on, and

$$C_\ell = \left\langle |a_\ell^m|^2 \right\rangle = \frac{1}{2\ell+1}\sum_m |a_\ell^m|^2\,. \tag{10.8}$$

3

In this way, the correlation function $C(\theta)$ can be broken down into its multipole components C_ℓ.

For a given CMB set of data (either an all sky map obtained by a satellite mission, or an observation over a more restricted portion of the sky from one of the ground-based experiments), it is possible to measure C_ℓ for angular scales larger than the resolution of the data and smaller than the patch of sky examined. Generally speaking, a term C_ℓ is a measure of $\delta T/T$ on the angular scale $\theta \sim 180°/\ell$.

The $\ell = 0$ term of the correlation function (the monopole) vanishes if the mean temperature has been defined correctly. The $\ell = 1$ term (the dipole) reflects the motion of the Earth through space, as we shall see in a moment. The moments with $\ell \geq 2$ are the ones of interest here, as they represent the fluctuations present at the time of last scattering.

The *power spectrum* of temperature fluctuations of the CMB is usually plotted as:
$$\Delta_\mathrm{T}^2 \equiv \frac{\ell(\ell+1)}{2\pi} C_\ell \ \langle T \rangle^2 \tag{10.9}$$
as a function of multipole moment ℓ ; the units of Δ_T^2 are $\mu\mathrm{K}^2$. The most precise determination of Δ_T over the largest range of scales has been provided by the Planck mission and is reproduced in Figure 10.2.

10.2   Dipole

The CMB map shown in Figure 10.1 has undergone several stages of processing in order to highlight the inherent temperature fluctuations imprinted on the CMB at the epoch of decoupling. First of all, foreground emission produced within the Milky Way has been subtracted out. Such emission is caused mostly by a combination of synchrotron radiation (produced by relativistic electrons spiralling in a magnetic field) and thermal emission from interstellar dust grains. This signal has value in its own right, but is a 'nuisance' factor if we are interested primarily in the CMB itself.

Once the foreground has been subtracted, we are left with an obvious dipole pattern, shown in Figure 10.3: the CMB temperature is slightly higher than
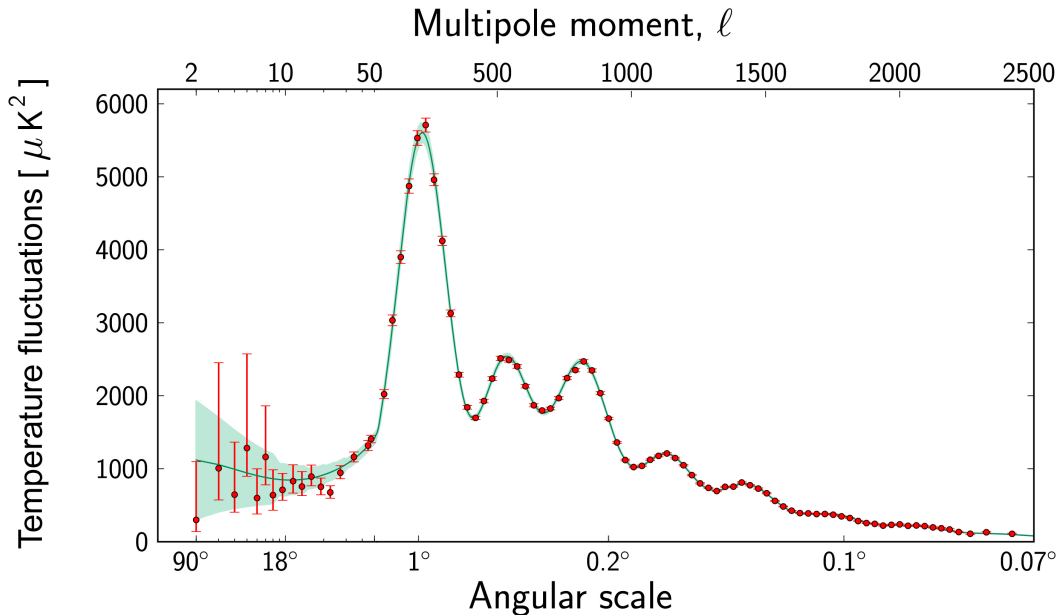
Figure 10.2: Power spectrum of the temperature fluctuations of the Cosmic Microwave Background measured by the Planck satellite. The red points are the measurements of Δ_{T}^2 as defined in eq. 10.9, with error bars that become larger at the largest scales because there are fewer pairs of directions, $\mathbf{r}$ and $\mathbf{r}'$, separated by such large values of θ on the sky. This is what is often referred to as 'cosmic variance'. The green curve is the best fit to the data obtained with the parameters that the define the 'standard model' of cosmology. The pale green area around the curve illustrates the predictions from the range of values of these parameters consistent with the Planck data.

average in a certain direction and slightly lower in the opposite direction on the sky. As can be seen from Figure 10.3, this temperature fluctuation is $\left\langle (\delta T/T)^2 \right\rangle^{1/2} \simeq 1 \times 10^{-3}$.

What we are seeing is the effect of the Earth's motion relative to the local comoving frame of reference. The Earth is moving with a velocity $v = 369\,\mathrm{km\ s^{-1}}$ towards a point on the boundary of the constellations of Crater and Leo. Consequently, our view of the CMB is redshifted (or blueshifted), depending on the angle θ relative to this direction, with a corresponding temperature shift such that:

$$T(\theta) \approx \langle T \rangle \left(1 + \frac{v}{c} \cos \theta \right). \tag{10.10}$$

The CMB dipole is a demonstration that we are not *fundamental observers* (recall the discussion in Lecture 1.1). After correcting for the orbital motions of: (i) the Earth around the Sun, (ii) the Sun relative to nearby stars, (iii) the solar neighbourhood around the centre of the Milky Way Galaxy, and (iv) the Milky Way relative to the centre of mass of the Local Group of
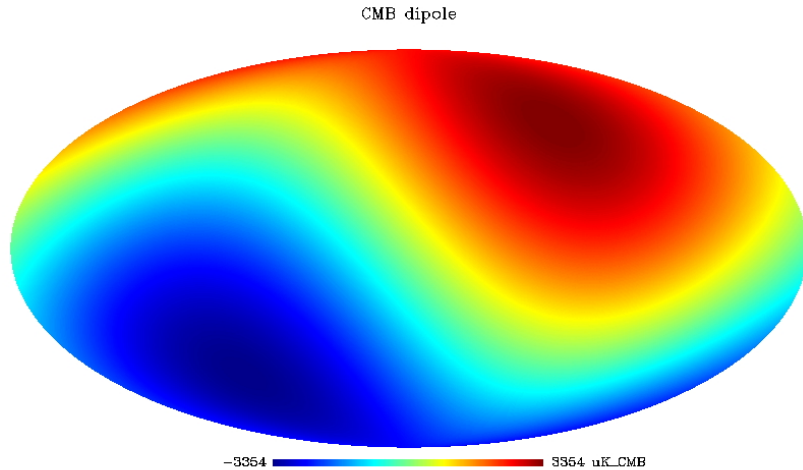
CMB dipole

−3354 ▮▮▮▮▮▮ 3354 uK_CMB

Figure 10.3: The CMB dipole, caused by the motion of the Earth relative to the Hubble flow. The CMB temperature is $3.35\,\mathrm{mK}$ higher than the mean in the direction with Galactic coordinates $l = 264°$ and $b = +48.4°$, and $3.35\,\mathrm{mK}$ lower in the opposite direction in the sky. Between these two directions there is a smooth variation between the maximum and minimum temperatures.

Galaxies, we find that the Local Group is itself being accelerated towards our nearest supercluster (of which the Virgo cluster is an outlying member) with a velocity $v_{\mathrm{LG}} = 630\,\mathrm{km\ s^{-1}}$.

It is also possible to calculate the net gravitational attraction acting on the Local Group by mapping the three-dimensional location of galaxies within a large volume around us (i.e.$\sim 200\,\mathrm{Mpc}$) from their celestial coordinates and redshifts. This exercise produces a dipole that is in good agreement, in both magnitude and direction, with that of the CMB, lending support to the interpretation of the CMB dipole as a doppler shift. The mass required to supply the gravitational attraction inferred corresponds to $\Omega_{\mathrm{m},0} = 0.31\pm 0.05$. The finding that $\Omega_{\mathrm{m},0} \simeq 6\,\Omega_{\mathrm{b},0}$ is another line of evidence for the existence of non-baryonic dark matter.

10.3   Higher Multipoles

We now return to the power spectrum of the primary temperature fluctuations (TT) shown in Figure 10.2. The y-axis of this plot shows the contribution per logarithmic interval in ℓ to the total temperature fluctuation δT of the CMB. Another way to think of this plot is that it shows the angular coherence of the temperature fluctuations. The CMB TT power spectrum shows an obvious peak at an angular scale $\theta \simeq 1°$ which, as we

6

shall now see, corresponds to the *sound horizon* at the time of decoupling.

Recalling some of the material covered of Lecture 9, at the epoch of recombination the Universe consisted of photons, protons, electrons, He nuclei, neutrinos and dark matter. The baryons and the photons are tightly coupled by Thomson and Coulomb scattering, while neutrinos (which are not relevant to our discussion here) and dark matter (which is relevant) are decoupled as they only interact via the weak nuclear force and gravity respectively. Thus, we speak of a baryon-photon fluid, whose energy density is dominated by radiation and can thus be treated as a relativistic fluid.[1]

The key thing here is that the baryon-photon fluid has a pressure, supplied by the photons. The fluid finds itself in gravitational potential wells (provided mostly by the dark matter); these are the 'seeds' that over the following 13.8 Gyr will evolve into the large-scale structure of the Universe. As gravity tries to compress the fluid, radiation pressure resists, eventually reversing the compression and causing the fluid to expands until gravity takes over again. This process results in an oscillating sequence of compressions and rarefactions. By analogy to the process in air where a travelling compressional wave is perceived as sound, we call these oscillations in the photon-baryon fluid acoustic oscillations. After all, sound is a travelling change of pressure.
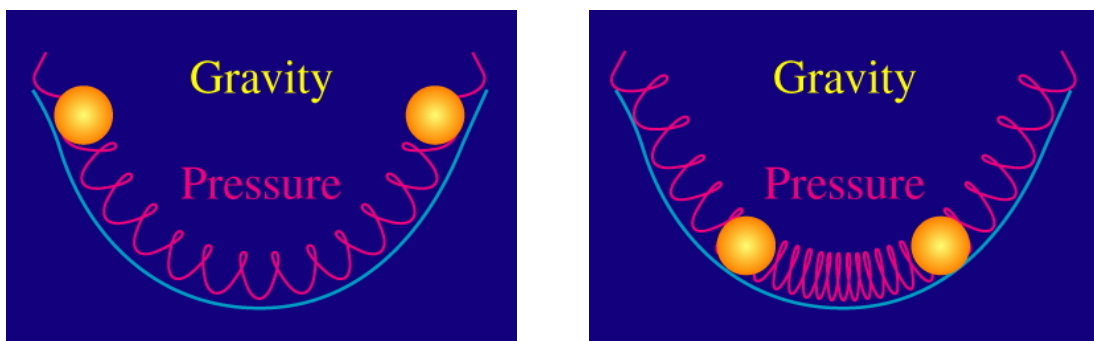

Figure 10.4: Radiation pressure (represented here by the spring) opposes the pull of gravity on the photon-baryon fluid (represented by the orange balls) falling into the potential wells of dark matter. (Figure credit: Wayne Hu).

The photon-baryon fluid stops oscillating at decoupling, when the baryons release the photons. The pattern of maxima and minima in the density is

---

[1]Even though we are in the matter dominated era, the energy density of the photons at z_{dec} exceeds that of the *baryons*, because $\Omega_{\mathrm{b},0} \simeq 1/6\,\Omega_{\mathrm{m},0}$, and this ratio has remained fixed since baryogenesis at $t \sim 10^{-35}$ s.

frozen in at that point, and preserved in the temperature fluctuations of the CMB. If the photon-baryon fluid within a dark matter potential well is at maximum compression at the time of photon decoupling, its (energy) density u will be higher than average and, recalling that for blackbody photons $u = a\,T^4$, the liberated photons will be hotter than average. Viceversa regions corresponding to maximum expansion will be slightly cooler than average.

So, modes caught at extrema of their oscillations become the peaks in the CMB power spectrum, often referred to as the acoustic peaks or Doppler peaks. They form a harmonic series based on the distance sound can travel by recombination, called the sound horizon. The first peak represents the mode that compressed once inside potential wells before recombination, the second the mode that compressed and then rarefied, the third the mode that compressed then rarefied then compressed, and so on.

The angular scales and amplitudes of the acoustic peaks are the main route to determining the cosmological parameters encoded in the temperature anisotropy of the CMB. The first example we consider is the value of ℓ of the first peak.

10.3.1 The First Doppler Peak: a Measure of the Curvature of the Universe

We have already considered the size of the horizon at z_{dec} in Lecture 9.4.1, where we deduced that:

$$s_{\mathrm{hor,prop}}(z_{\mathrm{dec}}) \simeq 2\frac{c}{H_0}\,\Omega_{\mathrm{m},0}^{-1/2}(1 + z_{\mathrm{dec}})^{-3/2}\,. \tag{10.11}$$

That was for photons, travelling at speed c. Here we are concerned with sound waves, travelling at speed c_{s}, defined as:

$$c_{\mathrm{s}}^2 = \frac{dp}{d\rho} \tag{10.12}$$

(Newton-Laplace equation). Pressure and density are related by the equation of state, already encountered in Lecture 6.4:

$$p = w\rho\,c^2 \tag{10.13}$$

with $w = 1/3$ for radiation. Thus, $c_s = \sqrt{1/3}\,c$, and the sound horizon (proper) at decoupling is therefore:

$$s_{\text{hor,s}} \simeq \frac{2}{\sqrt{3}} \frac{c}{H_0} \Omega_{\text{m,0}}^{-1/2} (1 + z_{\text{dec}})^{-3/2}\,. \tag{10.14}$$

The angle on the sky subtended by $s_{\text{hor,s}}$ depends on the angular diameter distance:

$$\theta_{\text{hor,s}} = \frac{s_{\text{hor,s}}}{d_A} \tag{10.15}$$

and d_A in turn depends on the cosmological parameters $\Omega_{\text{m,0}}$, $\Omega_{\text{k,0}}$, and $\Omega_{\Lambda,0}$ (with $\Omega_{\text{m,0}} + \Omega_{\text{k,0}} + \Omega_{\Lambda,0} = 1$) as we saw in Lecture 5. For the case $\Omega_{\Lambda,0} = 0$, we already saw in Lecture 9 (Mattig relation) that, at $z \gg 1$:

$$d_A(z) \approx 2 \frac{c}{H_0} \frac{1}{\Omega_{\text{m,0}}\, z}\,. \tag{10.16}$$

so that:

$$\theta_{\text{hor,s}} \simeq \frac{1}{\sqrt{3}} \left(\frac{(1 - \Omega_{\text{k,0}})}{z_{\text{dec}}} \right)^{1/2}\,. \tag{10.17}$$

From the above equation, it can be seen that as $\Omega_{\text{k,0}}$ increases from 0 to 1, $\theta_{\text{hor,s}}$ *decreases*, that is the first acoustic peak moves to larger ℓ values (see Figure 10.5).
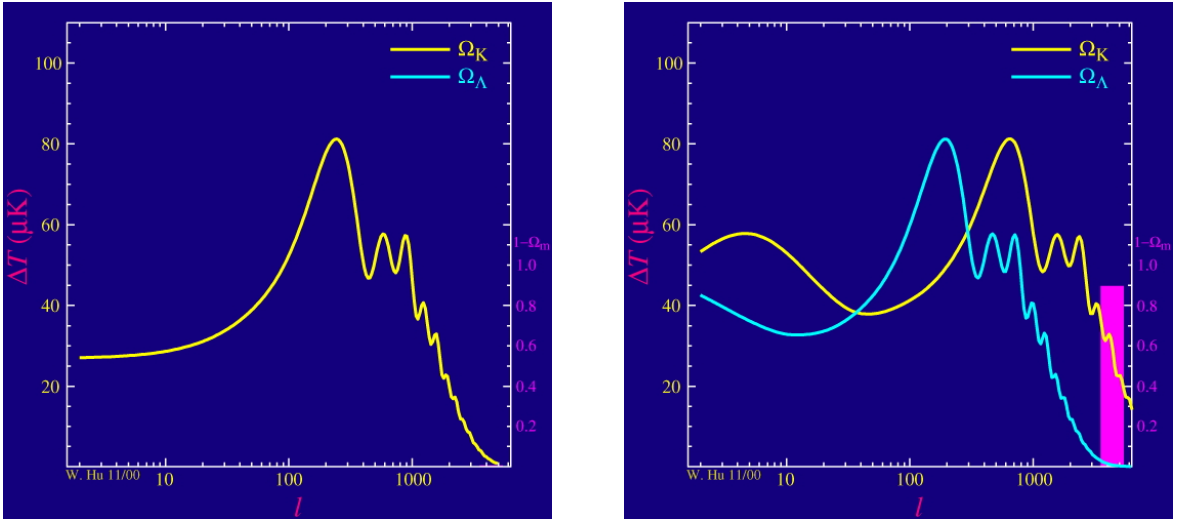

Figure 10.5: *Left:* CMB acoustic peaks expected for a cosmology in which $\Omega_{\text{k,0}} = 0$. *Right, Yellow Curve:* CMB acoustic peaks expected for a cosmology in which $\Omega_{\text{k,0}} = 0.9$. (Figure credit: Wayne Hu).
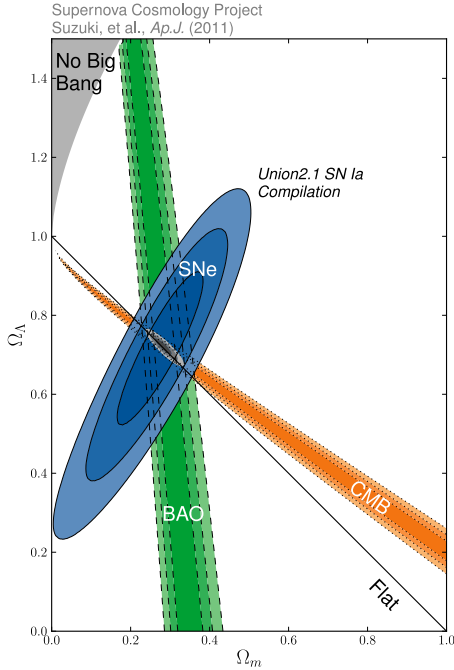
Figure 10.6: Joint likelihood contours (68%, 95%, and 99.7% confidence limits) in the $\Omega_{m,0} - \Omega_{\Lambda,0}$ plane for a recent compilation of SN Ia data, together with the WMAP measure of the temperature anisotropies of the CMB, and the large-scale distribution of galaxies in the nearby Universe (BAO).

In Lecture 9.4.1 we also saw that, in a $\Omega_{k,0} = 0$, $\Omega_{m,0} + \Omega_{\Lambda,0} = 1$ cosmology,

$$\theta_{\text{hor,dec}} \approx 1.8°$$

with a very weak dependence on $\Omega_{m,0}$ ($\propto \Omega_{m,0}^{-0.1}$ — see right panel of Figure 10.5). Thus, if we live in a flat Universe, we expect the location of the first Doppler peak to be at:

$$\theta_{\text{hor,s}} \approx \frac{1.8°}{\sqrt{3}} \simeq 1° \,,$$

and this is indeed the case (see Figure 10.2).

The size of the sound horizon at decoupling is often referred to as the much sought after *standard ruler*, from which cosmological parameters can be deduced via the angular diameter distance. In reality, many of the cosmological parameters that can be deduced from the analysis of the CMB TT power spectrum are to some extent degenerate with one another. Such degeneracies can be greatly reduced by combining CMB constraints with those derived from other considerations. We saw in Lecture 6 that the apparent magnitudes of distant Type Ia supernovae (essentially a luminosity distance test) delimit a region of the $\Omega_{\Lambda,0}$-$\Omega_{m,0}$ plane that is nearly orthogonal to that allowed by the CMB analysis (Figure 10.6). Thus, the combination of the two tests, one based on d_A and the other on d_L, is very powerful in constraining the allowed values of $\Omega_{m,0}$, $\Omega_{k,0}$, and $\Omega_{\Lambda,0}$ to a much tighter range than is possible with either test on its own.

10.4 Higher Doppler Peaks

The first acoustic peak defines a characteristic length-scale, corresponding to the sound horizon at decoupling. Fluctuations on larger scales are super-horizon, while fluctuations on smaller scales are sub-horizon, i.e. they were inside the horizon at decoupling and as such they were subject to physical effects acting on the baryon-photon fluid.

10.4.1 Baryon Loading: a Measure of $\Omega_{b,0}$

One such effect is termed *baryon loading*. Until now we have ignored the gravitational and inertial mass of the baryons; when this is taken into account, the fluid compresses further inside the potential well before pressure can reverse the motion. The oscillation is now asymmetric in that the extrema that represent compressions inside potential wells are increased over those that represent rarefactions. The effect on the power spectrum (where we plot Δ_T^2), is to increase the amplitudes of the compression peaks (odd-numbered peaks) relative to the amplitudes of the rarefaction (even-numbered) peaks.

A second consequence of baryon loading is that it decreases the frequency of the oscillations (the oscillations are slowed down by the baryons); this
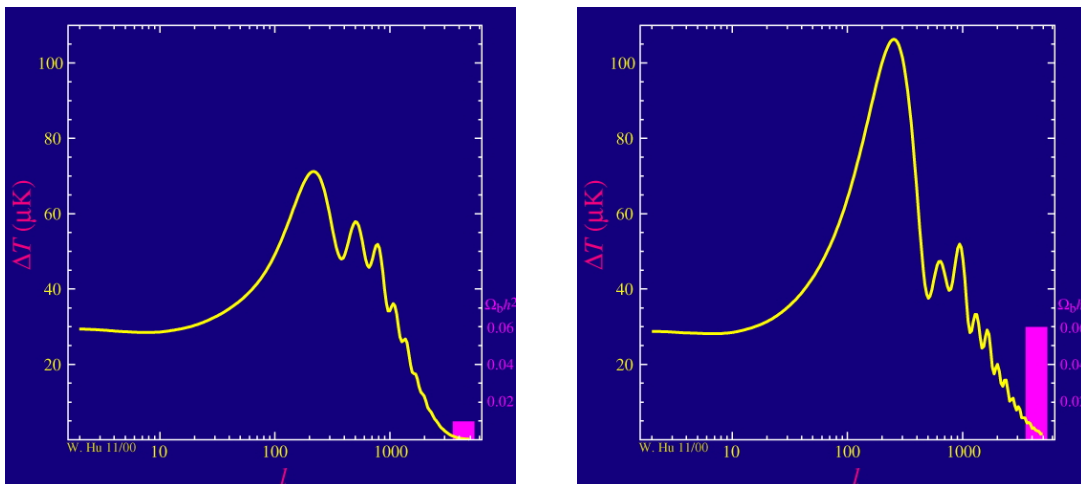

Figure 10.7: *Left:* CMB acoustic peaks if $\Omega_{b,0}h^2 = 0.01$. *Right:* CMB acoustic peaks if $\Omega_{b,0}h^2 = 0.06$. (Figure credit: Wayne Hu).

moves all the peaks to slightly higher multiples ℓ (see Figure 10.7). Baryons also affect the damping of the sound waves at high multiple moments, as we shall see presently.

Given the multiple effects that the presence of baryons has on the locations and amplitudes of the Doppler peaks of the CMB TT spectrum, the quantity $\Omega_{b,0}h^2$ is well determined from the analysis of the data in Figure 10.2: $\Omega_{b,0}h^2 = (2.226 \pm 0.016) \times 10^{-2}$, or $\Omega_{b,0}(\text{CMB}) = (4.884 \pm 0.035) \times 10^{-2}$ for $h = 0.675$. As already discussed in Lecture 8.5, this value is excellent agreement with that deduced from measurements of the primordial abundance of deuterium: $\Omega_{b,0}(\text{BBN}) = (4.91 \pm 0.11) \times 10^{-2}$. The finding that two measures of the same quantity based on entirely different physical processes—nuclear reactions at time $t \simeq 300\,\text{s}$ and acoustic oscillations of the baryon-photon fluid at time $t \simeq 372\,000\,\text{yr}$—are in such good agreement represents a remarkable success of the hot Big Bang theory of the Universe.

10.4.2   The Damping Tail

It is evident from Figure 10.2 that the angular coherence of the temperature fluctuations drops off at the smallest angular scales. This is a result of the fact that, as we approach the epoch of decoupling, the coupling between baryons and photons is not perfect: as the mean free path of photons grows, they can diffuse and smooth out temperature anisotropies on physical scales comparable to the distance travelled. As a result, the acoustic oscillations are exponentially damped on scales smaller than the distance photons random walk during the epochs of recombination and decoupling. This process is sometimes referred to as *Silk damping* after the British cosmologist who first proposed it in 1967 (only a few years after the CMB was discovered and many years before any anisotropies were identified).

Another way to look at this effect is as follows. We mentioned in Lecture 9.3 that decoupling was not an instantaneous process, and that it would be more appropriate to speak of a *last scattering layer*, rather than a *surface* of last scattering. Temperature fluctuations on physical scales smaller than the thickness of this layer (which is comparable to the photon mean free path) will be averaged out in the integration along the line of sight.
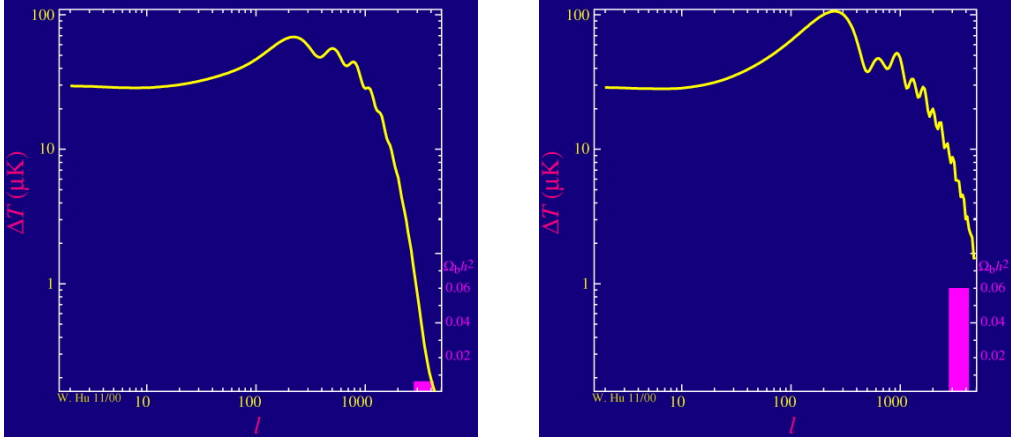
Figure 10.8: *Left:* CMB damping tail if $\Omega_{b,0}h^2 = 0.008$. *Right:* CMB damping tail if $\Omega_{b,0}h^2 = 0.06$. (Figure credit: Wayne Hu).

The shape of the damping tail of the power spectrum is sensitive to both $\Omega_{b,0}$ and $\Omega_{m,0}$, as can be seen from Figures 10.8 and 10.9 respectively. Since these parameters are also determined by the first few Doppler peaks, the exact shape of the damping tail provides a consistency check. Detailed numerical integration of the equations of motion is required to track the rapid growth of the mean free path and damping length near z_{dec}, and thereby match a given model to the data. Here we shall limit ourselves to a qualitative explanation.

The dependence on $\Omega_{b,0}$ is easier to understand. Increasing the baryon density makes the photon-baryon fluid more tightly coupled at recombination. The mean free path of the photons is shorter, and consequently the damping tail shifts to smaller angular scales. The total matter density
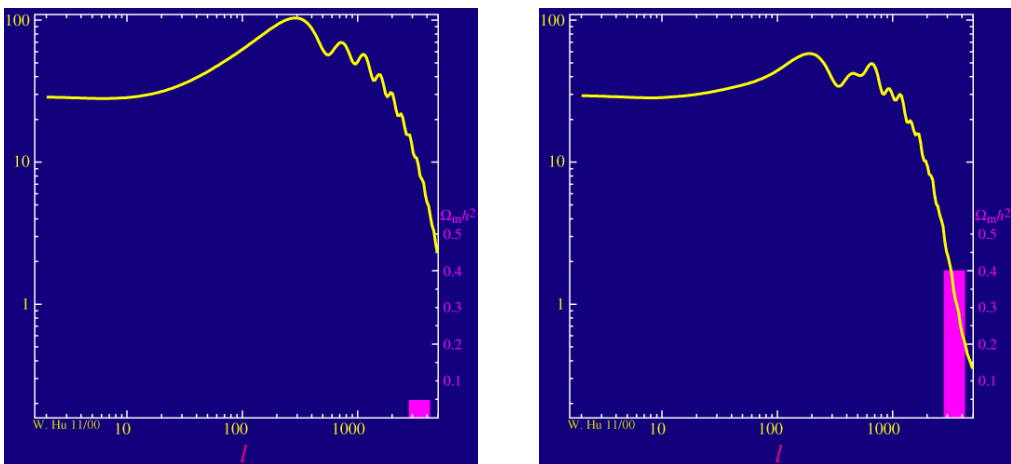

Figure 10.9: *Left:* CMB damping tail if $\Omega_{m,0}h^2 = 0.05$. *Right:* CMB damping tail if $\Omega_{m,0}h^2 = 0.4$. (Figure credit: Wayne Hu).

(dark matter + baryons) affects the damping tail through two factors: the age of the Universe at $z_{\rm rec}$, and the angular diameter distance $d_{\rm A}$ (both are smaller for larger values of $\Omega_{\rm m,0}$). The result is that a higher value of $\Omega_{\rm m,0}$ translates into more damping at a fixed multipole moment (see Figure 10.9).

10.5   Super-horizon Scales

We now focus on the interpretation of the CMB power spectrum on angular scales *larger* (i.e. smaller values of multiple moment ℓ) than the sound horizon at $z_{\rm dec}$. In this regime, the principal source of temperature fluctuations are the intrinsic inhomogeneities in the distribution of matter (mostly dark matter). Such inhomogeneities have their origin in quantum fluctuations stretched to cosmic scales during the inflationary era.

On angular scales greater than the *photon* horizon at $z_{\rm dec}$, i.e. $\theta > \theta_{\rm hor,dec} \gtrsim 1.8°$ (Lecture 9.4.1), the oscillations in the baryon-photon fluid (which move with the sound speed $c_{\rm s} = \sqrt{1/3}\,c$) are irrelevant, simply because there isn't enough time for the photon-baryon fluid to fall to the centre of the potential wells (or away from the potential peaks) by $z_{\rm dec}$. Fluctuations on these large scales reflect mainly the distribution of dark matter.

10.5.1   Sachs-Wolfe Effect

An energy density of dark matter that varies with position $\mathbf{r}$:

$$u_{\rm dm}(\mathbf{r}) = \langle u_{\rm dm} \rangle + \delta u_{\rm dm}(\mathbf{r}) \tag{10.18}$$

where $\langle u_{\rm dm} \rangle$ is the spatially averaged value of $u_{\rm dm}$ and $\delta u_{\rm dm}$ is the local deviation from the mean, generates a fluctuating gravitational potential $\delta\Phi$. $\delta u_{\rm dm}$ and $\delta\Phi$ are related by Poisson's equation:

$$\nabla^2(\delta\Phi) = \frac{4\pi G}{c^2}\,\delta u_{\rm dm}\,. \tag{10.19}$$

How do variations in the gravitational potential $\delta\Phi$ turn into temperature fluctuations $\delta T/T$? A detailed general relativistic calculation, performed

by Rainer Sachs and Arthur Wolfe in 1967 (hence the terminology of the Sachs-Wolfe effect) shows that:

$$\left(\frac{\delta T}{T}\right)_{\mathrm{S-W}} = \frac{1}{3}\frac{\delta\Phi}{c^2}\,. \tag{10.20}$$

There are two competing effects here. The first is that photons climbing out of potential well experience a gravitational redshift, and lose energy in the process (the opposite effect applies to photons who originated from 'potential hills', i.e. regions of lower density than the mean). From General Relativity, we know that for photons $\delta\nu/\nu = \delta\Phi/c^2$; since the blackbody shape remains unchanged, this translates directly to $\delta T/T = \delta\Phi/c^2$. Note that therefore regions of higher density (potential wells) will appear as 'cold spots' in the map of the CMB over the sky (Figure 10.1).

The second effect works in the opposite direction. Photons scattered from regions of higher density than average and received today were scattered at slightly earlier times, when the CMB temperature was slightly higher. The corresponding time interval is $\delta t/t = \delta\Phi/c^2$. Considering that: (i) in the matter dominated era, $a \propto t^{2/3}$; and (ii) $T_{\mathrm{CMB}} \propto a^{-1}$, we have: $\delta T/T = -2/3\,\delta t/t = -2/3\,\delta\Phi/c^2$. This time delay effect makes the potential wells appear slightly hotter than the mean in the CMB map, but doesn't quite compensate the gravitational redshift; in combination, they produce the Sachs-Wolfe effect of eq. 10.20.

Note that there is no scale dependence of the temperature fluctuations in eq. 10.20, and the Sachs-Wolfe effect appears as a constant Δ_{T}^2 in the power spectrum in Figure 10.2.[2] The value of Δ_{T}^2 at these large scales reflects directly the amplitude of the matter fluctuations at z_{dec}.

Note also from Figure 10.2 that the errors in the Planck determination of Δ_{T}^2 grow considerably as we move to angular scales $\theta \gg \theta_{\mathrm{hor,dec}}$, as does the range of values allowed by the combination of parameters that produce the best-fitting model (the pale green area in the plot). This is *cosmic variance*, an inherent uncertainty caused by the fact that there are only $2\ell + 1$ independent samplings we can make of our CMB sky at multiple moment ℓ. This translates into a limit to the precision achievable with

---

[2]As we shall see in Lecture 14, this reflects the scale invariant power spectrum of matter fluctuations expected from inflationary theory.

even a 'perfect' measurement of the C_ℓ modes in eq. 10.9:

$$\left(\frac{\Delta C_\ell}{C_\ell}\right)^2 = \frac{2}{2\ell + 1} \tag{10.21}$$

Hypothetically, If we were able to observe the CMB from a different location in the Universe (or communicate with observers in a different galaxy), we would be able to improve the statistics of the fluctuations on the largest scales.

10.5.2   Peculiar Velocities

Between the two scales, $\theta_{\mathrm{hor,rec}}$ and $\theta_{\mathrm{hor,s}}$, Δ_{T}^2 rises from the Sachs-Wolfe plateau to the first acoustic peak. What we are seeing here is just the effect of peculiar velocities relative to the Hubble flow—density fluctuations are always related to peculiar velocities of matter, as we have already seen when we discussed the CMB dipole in section 10.2. Thus, photons which were last scattered by gas receding from us with a speed slightly larger than the average Hubble expansion will experience an additional redshift which reduces the temperature measured in that direction (and conversely photons scattered by gas receding with a speed smaller than the Hubble flow will have a higher temperature).

The temperature fluctuations due to departures from uniform Hubble expansion introduce an additional term in eq. 10.20:

$$\left(\frac{\delta T}{T}\right)_{\mathrm{v,pec}} = \frac{1}{3}\frac{\delta \Phi}{c^2}\frac{\theta_{\mathrm{hor,rec}}}{\theta} \tag{10.22}$$

so that approximately $\Delta_{\mathrm{T}}^2 \propto \theta^{-1}$.

10.6   Primary Fluctuations: Conclusions

In conclusion, from the above discussion it should be clear that many parameters of interest to cosmologists are encoded in the power spectrum of temperature (and polarisation, which we have not touched upon) fluctuations of the cosmic microwave background. Many of the parameters

Table 4. Parameter 68 % confidence limits for the base ΛCDM model from *Planck* CMB power spectra, in combination with lensing reconstruction ("lensing") and external data ("ext," BAO+JLA+H_0). Nuisance parameters are not listed for brevity (they can be found in the *Planck Legacy Archive* tables), but the last three parameters give a summary measure of the total foreground amplitude (in μK^2) at $\ell = 2000$ for the three high-ℓ temperature spectra used by the likelihood. In all cases the helium mass fraction used is predicted by BBN (posterior mean $Y_P \approx 0.2453$, with theoretical uncertainties in the BBN predictions dominating over the *Planck* error on $\Omega_b h^2$).

Parameter	TT+lowP 68 % limits	TT+lowP+lensing 68 % limits	TT+lowP+lensing+ext 68 % limits	TT,TE,EE+lowP 68 % limits	TT,TE,EE+lowP+lensing 68 % limits	TT,TE,EE+lowP+lensing+ext 68 % limits
$\Omega_b h^2$	0.02222 ± 0.00023	0.02226 ± 0.00023	0.02227 ± 0.00020	0.02225 ± 0.00016	0.02226 ± 0.00016	0.02230 ± 0.00014
$\Omega_c h^2$	0.1197 ± 0.0022	0.1186 ± 0.0020	0.1184 ± 0.0012	0.1198 ± 0.0015	0.1193 ± 0.0014	0.1188 ± 0.0010
$100\theta_{MC}$	1.04085 ± 0.00047	1.04103 ± 0.00046	1.04106 ± 0.00041	1.04077 ± 0.00032	1.04087 ± 0.00032	1.04093 ± 0.00030
τ	0.078 ± 0.019	0.066 ± 0.016	0.067 ± 0.013	0.079 ± 0.017	0.063 ± 0.014	0.066 ± 0.012
$\ln(10^{10}A_s)$	3.089 ± 0.036	3.062 ± 0.029	3.064 ± 0.024	3.094 ± 0.034	3.059 ± 0.025	3.064 ± 0.023
n_s	0.9655 ± 0.0062	0.9677 ± 0.0060	0.9681 ± 0.0044	0.9645 ± 0.0049	0.9653 ± 0.0048	0.9667 ± 0.0040
H_0	67.31 ± 0.96	67.81 ± 0.92	67.90 ± 0.55	67.27 ± 0.66	67.51 ± 0.64	67.74 ± 0.46
Ω_Λ	0.685 ± 0.013	0.692 ± 0.012	0.6935 ± 0.0072	0.6844 ± 0.0091	0.6879 ± 0.0087	0.6911 ± 0.0062
Ω_m	0.315 ± 0.013	0.308 ± 0.012	0.3065 ± 0.0072	0.3156 ± 0.0091	0.3121 ± 0.0087	0.3089 ± 0.0062
$\Omega_m h^2$	0.1426 ± 0.0020	0.1415 ± 0.0019	0.1413 ± 0.0011	0.1427 ± 0.0014	0.1422 ± 0.0013	0.14170 ± 0.00097
$\Omega_m h^3$	0.09597 ± 0.00045	0.09591 ± 0.00045	0.09593 ± 0.00045	0.09601 ± 0.00029	0.09596 ± 0.00030	0.09598 ± 0.00029
σ_8	0.829 ± 0.014	0.8149 ± 0.0093	0.8154 ± 0.0090	0.831 ± 0.013	0.8150 ± 0.0087	0.8159 ± 0.0086
$\sigma_8\Omega_m^{0.5}$	0.466 ± 0.013	0.4521 ± 0.0088	0.4514 ± 0.0066	0.4668 ± 0.0098	0.4553 ± 0.0068	0.4535 ± 0.0059
$\sigma_8\Omega_m^{0.25}$	0.621 ± 0.013	0.6069 ± 0.0076	0.6066 ± 0.0070	0.623 ± 0.011	0.6091 ± 0.0067	0.6083 ± 0.0066
z_{re}	$9.9^{+1.8}_{-1.6}$	$8.8^{+1.7}_{-1.4}$	$8.9^{+1.3}_{-1.2}$	$10.0^{+1.7}_{-1.5}$	$8.5^{+1.4}_{-1.2}$	$8.8^{+1.2}_{-1.1}$
$10^9 A_s$	$2.198^{+0.076}_{-0.085}$	2.139 ± 0.063	2.143 ± 0.051	2.207 ± 0.074	2.130 ± 0.053	2.142 ± 0.049
$10^9 A_s e^{-2\tau}$	1.880 ± 0.014	1.874 ± 0.013	1.873 ± 0.011	1.882 ± 0.012	1.878 ± 0.011	1.876 ± 0.011
Age/Gyr	13.813 ± 0.038	13.799 ± 0.038	13.796 ± 0.029	13.813 ± 0.026	13.807 ± 0.026	13.799 ± 0.021
z_*	1090.09 ± 0.42	1089.94 ± 0.42	1089.90 ± 0.30	1090.06 ± 0.30	1090.00 ± 0.29	1089.90 ± 0.23
r_*	144.61 ± 0.49	144.89 ± 0.44	144.93 ± 0.30	144.57 ± 0.32	144.71 ± 0.31	144.81 ± 0.24
$100\theta_*$	1.04105 ± 0.00046	1.04122 ± 0.00045	1.04126 ± 0.00041	1.04096 ± 0.00032	1.04106 ± 0.00031	1.04112 ± 0.00029
z_{drag}	1059.57 ± 0.46	1059.57 ± 0.47	1059.60 ± 0.44	1059.65 ± 0.31	1059.62 ± 0.31	1059.68 ± 0.29
r_{drag}	147.33 ± 0.49	147.60 ± 0.43	147.63 ± 0.32	147.27 ± 0.31	147.41 ± 0.30	147.50 ± 0.24
k_D	0.14050 ± 0.00052	0.14024 ± 0.00047	0.14022 ± 0.00042	0.14059 ± 0.00032	0.14044 ± 0.00032	0.14038 ± 0.00029
z_{eq}	3393 ± 49	3365 ± 44	3361 ± 27	3395 ± 33	3382 ± 32	3371 ± 23
k_{eq}	0.01035 ± 0.00015	0.01027 ± 0.00014	0.010258 ± 0.000083	0.01036 ± 0.00010	0.010322 ± 0.000096	0.010288 ± 0.000071
$100\theta_{s,eq}$	0.4502 ± 0.0047	0.4529 ± 0.0044	0.4533 ± 0.0026	0.4499 ± 0.0032	0.4512 ± 0.0031	0.4523 ± 0.0023
f_{2000}^{143}	29.9 ± 2.9	30.4 ± 2.9	30.3 ± 2.8	29.5 ± 2.7	30.2 ± 2.7	30.0 ± 2.7
$f_{2000}^{143\times217}$	32.4 ± 2.1	32.8 ± 2.1	32.7 ± 2.0	32.2 ± 1.9	32.8 ± 1.9	32.6 ± 1.9
f_{2000}^{217}	106.0 ± 2.0	106.3 ± 2.0	106.2 ± 2.0	105.8 ± 1.9	106.2 ± 1.9	106.1 ± 1.8

Table 5. Constraints on 1-parameter extensions to the base ΛCDM model for combinations of *Planck* power spectra, *Planck* lensing, and external data (BAO+JLA+H_0, denoted "ext"). Note that we quote 95 % limits here.

Parameter	TT	TT+lensing	TT+lensing+ext	TT, TE, EE	TT, TE, EE+lensing	TT, TE, EE+lensing+ext
Ω_K	$-0.052^{+0.049}_{-0.055}$	$-0.005^{+0.016}_{-0.017}$	$-0.0001^{+0.0054}_{-0.0052}$	$-0.040^{+0.038}_{-0.041}$	$-0.004^{+0.015}_{-0.015}$	$0.0008^{+0.0040}_{-0.0039}$
Σm_ν [eV]	< 0.715	< 0.675	< 0.234	< 0.492	< 0.589	< 0.194
N_{eff}	$3.13^{+0.64}_{-0.63}$	$3.13^{+0.62}_{-0.61}$	$3.15^{+0.41}_{-0.40}$	$2.99^{+0.41}_{-0.39}$	$2.94^{+0.38}_{-0.38}$	$3.04^{+0.33}_{-0.33}$
Y_P	$0.252^{+0.041}_{-0.042}$	$0.251^{+0.040}_{-0.039}$	$0.251^{+0.035}_{-0.036}$	$0.250^{+0.026}_{-0.027}$	$0.247^{+0.026}_{-0.027}$	$0.249^{+0.025}_{-0.026}$
$dn_s/d\ln k$	$-0.008^{+0.016}_{-0.016}$	$-0.003^{+0.015}_{-0.015}$	$-0.003^{+0.015}_{-0.014}$	$-0.006^{+0.014}_{-0.014}$	$-0.002^{+0.013}_{-0.013}$	$-0.002^{+0.013}_{-0.013}$
$r_{0.002}$	< 0.103	< 0.114	< 0.114	< 0.0987	< 0.112	< 0.113
w	$-1.54^{+0.62}_{-0.50}$	$-1.41^{+0.64}_{-0.56}$	$-1.006^{+0.085}_{-0.091}$	$-1.55^{+0.58}_{-0.48}$	$-1.42^{+0.62}_{-0.56}$	$-1.019^{+0.075}_{-0.080}$

Figure 10.10: Cosmological parameters derived from the analysis of Planck data 2015.

have multiple effects on the shape and normalisation of the power spectrum, allowing internal consistency checks. Given sufficient precision in recording the intensity of the background over the sky (and in subtracting foregrounds and accounting for other systematics), now achieved with the Planck mission, the most important parameters describing our Universe have been determined with percent accuracy—a feat that would have been thought impossible half a century ago. Figure 10.10 is the final compilation of cosmological parameters deduced from the analysis of Planck data.

10.7   Secondary Fluctuations

On their way from the surface of last scattering to our detectors on Earth, the CMB photons are affected by a number of secondary effects which introduce additional anisotropies:

(i) *Thomson scattering* by free electrons in the intergalactic medium (IGM), following the so-called *epoch of reionisation*. This is when the widely distributed baryons in the Universe, which had remained neutral since z_{dec}, were reionised by the UV photons produced by the first stars. Scattering of CMB photons on IGM electrons essentially reduces the fluctuation amplitude on all scales by a factor $\mathrm{e}^{-\tau}$, where τ is the optical depth to Thomson scattering. From the magnitude of τ we can deduce z_{reion}, since the earlier reionisation occurred, the larger the optical depth to Thomson scattering.

The latest Planck results in conjunction with other data indicate $z_{\mathrm{reion}} = 8.5 \pm 1.3$ (see Figure 10.10). For comparison, the highest redshift galaxy known at present is at $z = 8.68$.

(ii) *Gravitational lensing*, whereby the gravitational field of the cosmic density fluctuations leads to changes in the photon direction. The result is that the correlation function of the temperature fluctuations is slightly smeared out on small angular scales.

(iii) *Integrated Sachs-Wolfe effect*, caused by the fact that the gravitational potential of the large-scale structure changes over timescales comparable to the travel time of CMB photons through the structures. This

is most important over the largest angular scales and when the Hubble expansion is accelerated by, for example, a cosmological constant. Accelerated expansion causes large-scale potential wells (superclusters) and 'peaks' (voids) to decay over the time it takes a photon to travel through them. Thus, the blueshift that a CMB photons undergoes as it travels down a potential well is not exactly balanced by a corresponding redshift as it climbs out (and vice versa).

(iv) *The Sunyaev-Zeldovich (S-Z) effect* produced by inverse Compton scattering of CMB photons by electrons in the intracluster gas of massive galaxy clusters.

Of these, we consider the S-Z effect in a little more detail below.

10.7.1 The Sunyaev-Zel'dovich Effect

Galaxy clusters are some of the largest concentrations of matter in the Universe and are interesting for many reasons, as we shall see later in the course. For the present purposes, it is sufficient to say that the richest

Figure 10.11: *Left:* The galaxy cluster Abell 1689 observed with the *Hubble Space Telescope* Advanced Camera for Surveys. This cluster is one of the largest concentrations of matter in the local Universe ($z = 0.1828$), with a mass $M \simeq 10^{15}\,\mathrm{M_\odot}$. *Right:* The X-ray image of the cluster (shown here superimposed on the *HST* image taken in visible light) obtained by the *Chandra* observatory shows diffuse emission from intracluster gas at temperatures $T \sim 10^8\,\mathrm{K}$.

galaxy clusters consist of thousands of galaxies (mostly ellipticals) within a volume of radius $R < 5\,\mathrm{Mpc}$. Most of the baryons, however, are not in galaxies, but in hot intracluster gas (ICM); galaxies and gas move within the same gravitational potential (supplied mostly by the dark matter). The intracluster gas is at very high temperatures, up to $T \sim 10^8\,\mathrm{K}$, and is therefore fully ionised. Its presence is revealed by its X-ray emission, both continuum emission (bremsstrahlung) and line emission from highly ionised atoms (see Figure 10.11).

Electrons in the ICM can transfer energy to CMB photons via *inverse Compton scattering* (a type of free-free emission). Even though the scattering changes the direction in which CMB photons travel, the isotropy of the cosmic background ensures that, on average, the total number of CMB photons reaching us is unchanged.

What changes is their frequency distribution, which now is slightly distorted relative to a perfect blackbody, as illustrated in Figure 10.12. In the Raleigh-Jeans part of the CMB spectrum (i.e. at wavelengths longer than $1\,\mathrm{mm}$), photons are effectively removed by the the SZ effect (and conversely in the Wien part of the spectrum the SZ effect boosts the CMB).
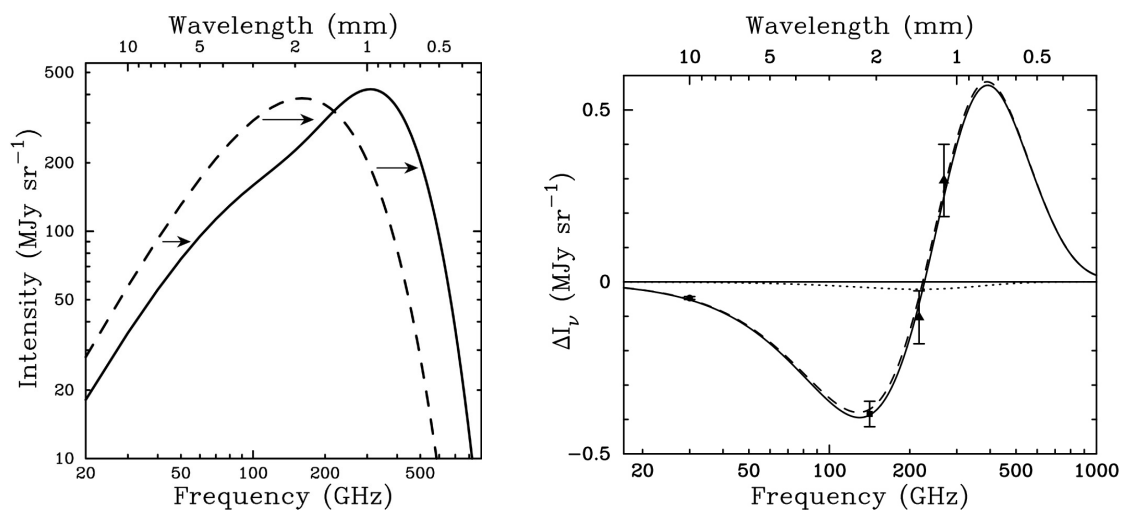

Figure 10.12: *Left:* Inverse Compton scattering by energetic electrons in the intracluster medium of massive galaxy clusters alters the blackbody spectrum of CMB photons travelling through the cluster (*dashed line*: intrinsic spectrum; *continuous line*: emerging spectrum). This is the Sunyaev-Zel'dovich effect, named from the two Russian cosmologists who predicted it in 1970. *Right:* Difference between the intensity of the CMB and the signal through the cluster of galaxies Abell 2163. ΔI_ν is negative at frequencies lower than $218\,\mathrm{Ghz}$ (wavelengths longer than $1.4\,\mathrm{mm}$), and positive at higher frequencies. (Figures reproduced from Carlstrom et al. 2002).

Calculation shows that the change in intensity can be related to the physical properties of the cluster:

$$\frac{\Delta I_\nu^{\mathrm{RJ}}}{I_\nu^{\mathrm{RJ}}} = -2y \tag{10.23}$$

and

$$y = \int \frac{kT}{m_{\mathrm{e}}c^2}\, \sigma_{\mathrm{T}}\, n_{\mathrm{e}}\, \mathrm{d}l \tag{10.24}$$

where $\sigma_{\mathrm{T}} = 6.65 \times 10^{-25}\,\mathrm{cm}^2$ is the cross-section for Thomson scattering (independent of photon frequency), T is the temperature of the ICM, and the other symbols have their usual meaning. The integration is carried out along the pathlength $\int \mathrm{d}l$ through the cluster. Note that the so-called *Compton y parameter* in eq. 10.24 increases with T, since the temperature determines the average energy transfer per scattering event. Overall, y is proportional to the integral of the *pressure* $(P = nkT)$ along the line of sight through the cluster. Typical values of $\Delta I_\nu/I_\nu$ at $30\,\mathrm{GHz}$ $(1\,\mathrm{cm})$ correspond to $\Delta T/T \leq 1\,\mathrm{mK}$.

Note also that the drop in intensity, $\Delta I_\nu/I_\nu$, is independent of redshift and of the details of the gas distribution within the cluster. Thus, the S-Z effect is a useful tool for the identification of clusters at high redshifts, free from many selection effects (see Figure 10.13). By assembling samples of galaxy clusters at different redshifts we can follow the growth of structure over a substantial fraction of cosmic time.

Furthermore, spatially resolved maps such as those reproduced in Figure 10.13 give information about the temperature and density distribution of the gas within a cluster, complementing analogous data obtained from the X-ray emission. Finally, the combination of the S-Z decrement and X-ray emission has been used to deduce cluster distances. This is one of the many avenues to the determination of the Hubble parameter H_0, as we shall see later in the course.
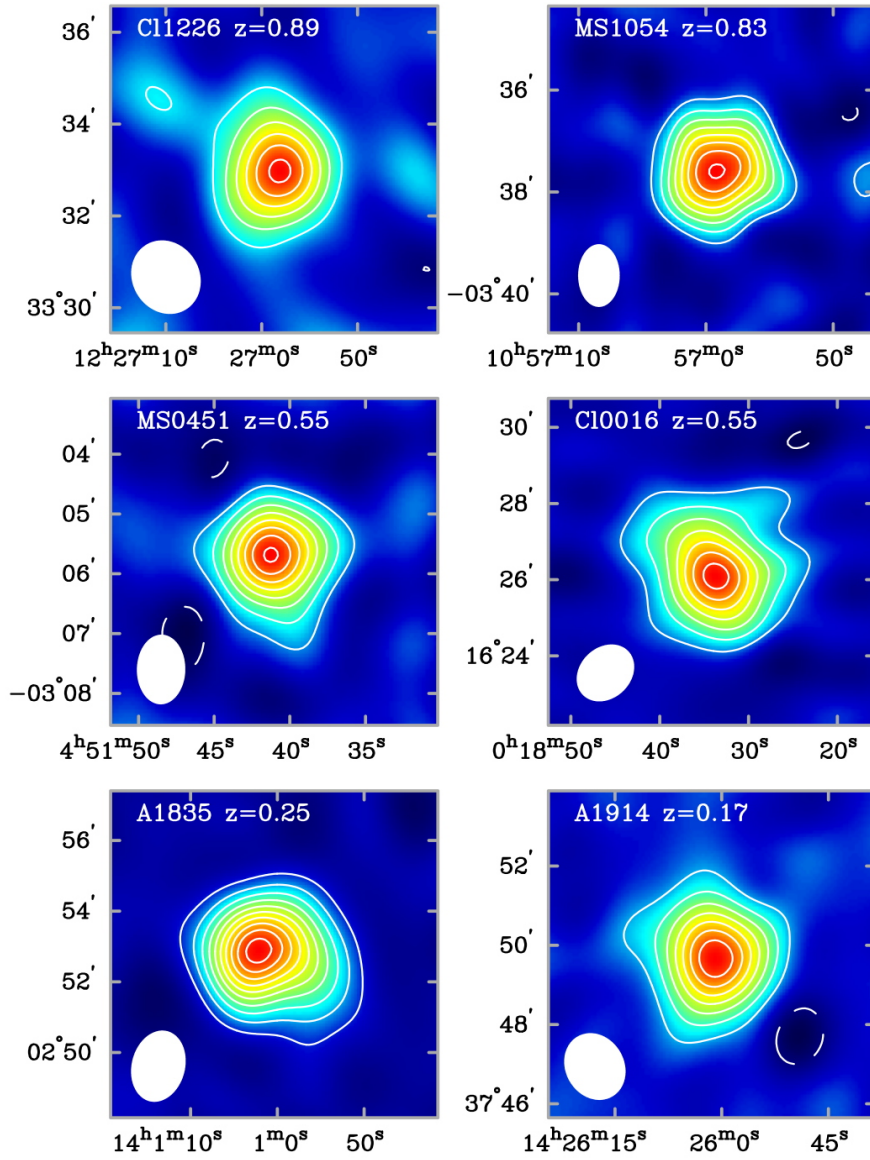
Figure 10.13: S-Z effect in six clusters at different redshifts, from $z = 0.17$ to $z = 0.89$. The colour coding is such that red corresponds to the largest values of $|\Delta I_\nu / I_\nu|$ and blue to the lowest. The strength of the S-Z signal falls off from the core to the outskirts of each cluster, reflecting the decrease of the integral $\int n_e T \, dl$ with projected distance from the centre. All of the clusters shown have similar high X-ray luminosities and, as can be seen, the strengths of their S-Z signals are similar, illustrating the independence of the S-Z effect on redshift. These images were obtained with the Owens Valley Radio Observatory at a frequency of $30\,\text{GHz}$ ($\lambda = 1\,\text{cm}$). (Figure reproduced from Carlstrom et al. 2002).